Energy Advances

ROYAL SOCIETY OF CHEMISTRY

PAPER

View Article Online
View Journal

Cite this: DOI: 10.1039/d5ya00374a

Carbon-coated niobium tungsten oxides as new and efficient anode materials for Na-ion batteries

Y. Bhaskara Rao,* Katta Vamsi Krishna and C. André Ohlin*

Tetragonal tungsten bronze (TTB)-type niobium–tungsten oxides are very interesting anode candidates for Na-ion battery applications due to their compositional flexibility, structural stability and large open-tunnel networks, which enable fast ion transport and pseudo capacitive behaviour. The present work introduces two TTB-type niobium tungstate anode materials, namely $Nb_{18}W_{16}O_{93}$ (Nb dominant) and $Nb_7W_{10}O_{47}$ (W dominant), prepared by a one-step hydrothermal method followed by low-temperature calcination at 800 °C. Furthermore, the low inherent electronic conductivity of the anode materials is effectively enhanced by incorporating the active materials with a carbon matrix to improve Na^+-ion transport and storage. The presence of uniform carbon-coating surrounding the active particles in both materials is confirmed by high-resolution transmission electron microscopy images. At a current density of 10 mA g^{-1}, carbon-coated $Nb_{18}W_{16}O_{93}$ (NWO) delivered a higher reversible capacity of 163.95 mA h g^{-1} compared to that of carbon-coated $Nb_7W_{10}O_{47}$ (WNO) (127.55 mA h g^{-1}). Interestingly, the WNO material showed remarkable cycling stability over 420 cycles, at a current density of 100 mA g^{-1}, recording a higher capacity retention of 81%, compared to NWO (69%). The promising electrochemical performance of the materials is related to structural defects, specific surface areas, charge transfer resistances during charge/discharge cycles and Na^+-ion diffusion coefficients. Thus, the current work introduces niobium tungsten oxides as new and efficient anode candidates for sodium ion battery technology, and also enables safe, economical, and long-cycling Na-ion batteries, ultimately supporting the transition toward more sustainable energy technologies.

Received 22nd December 2025,
Accepted 14th April 2026

DOI: 10.1039/d5ya00374a

rsc.li/energy-advances

1. Introduction

Sodium-ion batteries (SIBs) have several intrinsic advantages over lithium ion batteries (LIBs), making them promising in large-scale energy storage systems (ESSs) as sodium is cheaper and more readily available than lithium.[1,2] The majority of SIB research has been devoted to investigating stable and inexpensive cathode materials, such as Prussian blue, $NaFePO_4$, and $NaNi_{0.5}Mn_{0.5}O_2$.[3,4] Most of the ongoing efforts to explore anode materials are limited to non-graphitic carbonaceous materials. Because of its disordered structure and high interlayer distance, hard carbon is currently the best non-graphitic carbonaceous material for Na^+-ion storage.[5] Nonetheless, non-graphitic carbonaceous materials have certain drawbacks, including a high irreversible capacity and low capacity retention.

Metal oxides have been investigated and developed widely as alternatives to carbon-based anodes in SIBs due to their high theoretical capacity.[6] Among them, oxides based on niobium are of great interest, due to their better physicochemical characteristics and potential usage in energy-storage devices. In addition, they have a high working potential (>1.0 V) that can inhibit the formation of sodium dendrites and ensure the safety of operational batteries.[7] Nevertheless, the low intrinsic electrical conductivity of many niobium-based oxides (*ca.* 3.4×10^{-6} S cm^{-1} at 300 K) decreases the alkali ion diffusion rate and restricts their application as substitutes for commercial anode materials.[8] The carbon coating of the active material is found to be an economically feasible, simple, and practical method among the different approaches investigated to improve the electronic conductivity.[9]

Several studies have reported the incorporation of a carbon matrix around active particles to improve the electronic conductivity, thereby enhancing the electrochemical performance of the materials. For instance, our group recently reported a solution-assisted solid-state process to prepare fluorine-doped and carbon-coated KNb_3O_8 material, which delivered a discharge capacity of 173 mA h g^{-1} at a current density of 10 mA g^{-1}.[10] In this case, polyvinylidene fluoride (PVDF), a commonly used binder in SIBs/LIBs, is used as both a carbon and a fluorine source. Chen *et al.* reported a composite of TT-Nb_2O_5 and CNT (glucose-derived carbon) synthesized by a one-step hydrothermal method, followed by annealing. The material delivered a high specific capacity of 203 mA h g^{-1} at 0.2 A g^{-1} and a capacity

Department of Chemistry, Umeå University, Umeå, 90187, Sweden.
E-mail: bhaskararaoyenduri@gmail.com, andre.ohlin@umu.se

retention of ~ 135 mA h g^{-1} at 0.2 A g^{-1} after 300 cycles.[11] Using polyacrylonitrile as a carbon and nitrogen source, a sonochemical method was employed to prepare core–shell structured Nb_2O_5@NC nanoparticles.[12] After 200 cycles at 0.2 C the nanocomposite exhibited a discharge capacity of 96 mA h g^{-1}, which is a notable improvement over the undoped sample (28 mA h g^{-1}).

Here we report niobium tungsten oxide materials as new anode candidates in SIBs for the first time. The benefits of niobium tungsten oxide anodes include long-term capacity retention and high energy and power densities. Additionally, they offer enhanced electrochemical performance as well as improved safety at low temperatures.[13] These advantages result from stable crystal structures and excellent mobile-ion diffusion coefficients. Generally, niobium oxides are known for their robust frameworks and pseudo capacitive sodium-storage behavior but suffer from limited electronic conductivity, whereas tungsten oxides exhibit relatively higher electronic conductivity yet inferior structural stability during cycling. The combination of Nb and W within a single oxide framework effectively integrates the advantages of both components, leading to improved charge transport and electrochemical kinetics. Furthermore, incorporating tungsten into the niobium oxide framework offers a promising strategy to enhance the electronic transport and stabilize open crystallographic shear structures.[14] However, systematic studies correlating the crystallographic shear architecture of niobium–tungsten oxides with Na-storage kinetics remain scarce. This work addresses this gap by investigating representative Nb–W–O shear phases and elucidating their structure–property–performance relationships in Na^+-ion batteries. In this work, two niobium tungsten oxide materials, $Nb_{18}W_{16}O_{93}$ (Nb rich) and $Nb_7W_{10}O_{47}$ (W rich), were chosen to investigate the influence of Nb and/or W on the overall performance of the SIB half cells. Both belong to pseudo-tetragonal tungsten bronze orthorhombic superstructures, which generally consist of corner-sharing octahedra (MO_6) arranged in such a way that trigonal, square, and pentagonal tunnels arise.[15] The Nb-rich phase contains partially occupied pentagonal tunnels with metal–oxygen strings, whereas the W-dominant phase contains more open or less occupied tunnels resulting from its higher oxygen content compared to the Nb-richer phases.[16] The availability of sites for ion storage and improved diffusion speed is directly affected by the degree to which these tunnels are occupied, with the main difference between the two structures lying in their oxygen-to-metal ratio, which ultimately decides the occupation of mobile-ion diffusion channels within their shared tetragonal tungsten bronze (TTB)-type framework.

The two materials $Nb_{18}W_{16}O_{93}$ and $Nb_7W_{10}O_{47}$ are prepared by a simple hydrothermal method followed by low-temperature calcination. Although 800 °C is high in absolute terms, for this niobium tungsten oxide system, this method represents a relatively mild lower-temperature route compared to traditional solid-state methods (>1000 °C), which is beneficial for energy savings and suppressing excessive grain growth. Previous studies have shown that niobium-rich Nb–W bronze structures can be achieved by synthesizing the materials at 800–900 °C, demonstrating that complex Nb–W oxides can form at these moderate temperatures without the need for much higher (>1000 °C) processing.[17] Furthermore, both materials are coated with carbon, using sucrose as a carbon source, as it is easily soluble in water without affecting the pH, inexpensive, and yields uniform carbon coatings on inorganic particles upon pyrolysis,[18] which further improve the electrochemical performance of the electrodes. The structure, morphology, specific surface area, disordered/defective nature, Na^+-ion diffusion coefficient, and the contribution of capacitive and diffusive behaviour are all examined in this work and compared in relation to the transport and storage behaviour of Na^+ ions in the materials. X-ray diffraction (XRD), scanning electron microscopy (SEM), and transmission electron microscopy (TEM) were used to investigate the crystalline structure and morphology of the samples, respectively. Raman spectroscopy was used to study the vibrational modes as well as the D and G bands. Furthermore, N_2 adsorption/desorption isotherms were utilized to analyze the specific surface area and pore size distributions. Cyclic voltammetry (CV), galvanostatic charge/discharge cycles, Nyquist impedance plots and the total capacitance partition curves were employed to study the electrochemical performance of the materials.

2. Experimental section

2.1 Material synthesis

Carbon-coated $Nb_{18}W_{16}O_{93}$ and $Nb_7W_{10}O_{47}$ (nominal composition: $Nb_7W_{10}O_{47.5}$) materials were prepared by a simple hydrothermal method followed by calcination. In a typical reaction, stoichiometric ratios of niobic acid ($Nb_2O_5{\cdot}nH_2O$, >99%, 40% H_2O w/w; received as a gift from Prof. William H. Casey at UC Davis) and tungsten oxide (WO_3, 99.9%, TCI) were mixed with sucrose ($C_{12}H_{22}O_{11}$, >99%, TCI, 1 g) in 50 ml of de-ionized water in a Teflon liner. It was then magnetically stirred for 1 h prior to heating at 180 °C for 12 h. After cooling to room temperature, the product was filtered and dried at 100 °C in a drying oven. Finally, the material was calcined at 800 °C for 4 h under a N_2 atmosphere to obtain the final carbon-coated $Nb_{18}W_{16}O_{93}$ and $Nb_7W_{10}O_{47}$ samples. These carbon-coated samples were then referred to as NWO (Nb-rich) and WNO (W-rich), respectively.

2.2 Material characterization

XRD was performed with a Bruker D8 Advance diffractometer using Cu-K_α radiation and the LYNXEYE XE-T detector model operated at 40 kV/40 mA in the 1D mode to analyze the crystal structure of the materials. The samples were scanned at a step size of 0.01945° in the 2θ range of 10–80°. The Raman spectra were recorded using a Renishaw Qontor device (Renishaw Plc, UK) running WiRe (version 5.6). Using a 5× lens in the normal confocality mode, a 405 nm solid state laser with a nominal maximum power of 40 mW was employed. The spectral range was centered at 1400 cm^{-1}, and 10 s exposure times were used. SEM images were obtained using a Zeiss Evo SEM instrument equipped with an HDBSD detector. The energy-dispersive X-ray spectroscopy (EDX) images were taken with the help of an X-MaxN 80 mm^2 silicon drift detector. FEI Glacios 200 kV

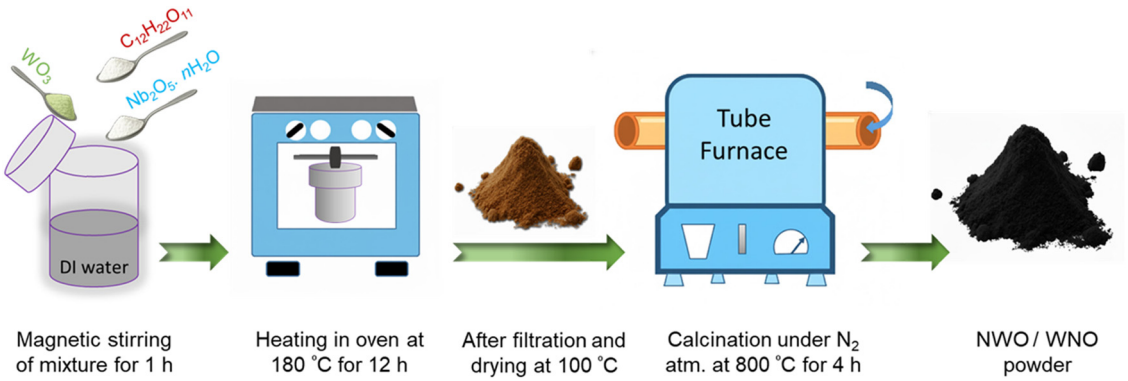

Fig. 1 Schematic diagram for the preparation of NWO/WNO samples.

cryo-TEM with a Ceta-D 4k × 4k CMOS detector was used to get the TEM images, and the TEM grids were obtained using a Quantifoil R2/1 micro machined holey carbon grid (300 mesh copper). For selected area electron diffraction (SAED) pictures, an aperture of 10 μm was used. A Micromeritics TriStar 3000 porosimeter was used to measure N_2 adsorption–desorption and the isotherms were recorded at −196 °C after the samples were outgassed for two hours at 100 °C. The specific surface areas were obtained using the Brunauer–Emmett–Teller (BET) method, and the pore volumes were computed using the desorption isotherms. The pore size distributions were estimated using the Barret, Joyner, and Halenda (BJH) algorithm and the ASAP-2010 program.

2.3 Electrochemical characterization

CR-2032 coin-type half-cells were prepared for the electrochemical experiments in an Ar-filled glove box (Mbraun, MB10 compact) with O_2 and H_2O levels <0.5 ppm. The active material (80 wt%), Super P (Thermo Scientific) (10 wt%), and sodium carboxymethyl-cellulose (CMC-MedChemExpress; 10 wt%) binder were mixed with de-ionized water to prepare a slurry. After applying the mixture on a copper foil current collector (TMAXCN; 14 mm in diameter and 0.1 mm in thickness), it was dried at 50 °C. The electrode had an average mass loading of 2–3 mg cm^{-2}. The liquid electrolyte was 1 M $NaClO_4$ (Thermo Scientific) in ethylene carbonate (EC, from AmBeed) and dimethyl carbonate (DMC, from TCI; 1 : 1 v/v), and the separator was a glass microfibre filter (Whatman, Grade GF/D; 19 mm diameter). The counter/reference electrode was Na metal. A Solartron Modulab 2100A workstation was used to record the CV curves (0.01–2.5 V) at different scan rates and electrochemical impedance spectroscopy (EIS) spectra in the frequency range of 100 mHz to 100 kHz. The galvanostatic charge–discharge curves were recorded using a NEWARE CT-4008 battery tester within a voltage window of 0.01–2.5 V (*vs.* Na^+/Na). Every electrochemical measurement was performed at 20 °C.

3. Results and discussion

The schematic of the synthesis of niobium tungsten oxides *via* a simple hydrothermal method followed by low-temperature calcination (800 °C) is shown in Fig. 1.

Fig. 2a and b display the XRD patterns of the materials, NWO and WNO, and the sharp diffraction peaks indicate that both materials have good crystallinity. Major reflections of the NWO sample are associated with the distorted TTB crystal structure with the *Pbam* space group ($Nb_{18}W_{16}O_{93}$ – COD# 2107344).[19] While, the reflections of the sample WNO are related to an orthorhombic crystal structure with the $P2_12_12$ space group ($Nb_7W_{10}O_{47}$ – COD# 1521454),[20] and a minor intermediate tetragonal phase, $Nb_{0.24}W_{1.76}O_{5.88}$ (COD# 1522265) is also observed in both of the materials. Furthermore, the reference patterns of Nb_2O_5 (COD# 2106534) and WO_3 (COD# 1004057) are presented in Fig. 2a and b for comparison. The orthorhombic NWO is a 1 × 3 × 1 superstructure of the typical tetragonal tungsten bronze (Fig. 2c). In addition to the distorted octahedra of the tetragonal tungsten bronzes, the superstructure is produced by partially filling pentagonal tunnels with –M–O– chains to form pentagonal bipyramids.[13] On the other side, an important feature of the WNO structure (Fig. 2d) is that the pentagonal tunnels are nearly regular pentagons when they are occupied by M–O chains, whereas the unoccupied pentagonal tunnels are much more deformed.[20] The trigonal (t), square (s), and pentagonal (p) tunnels emerging from the arrangement of corner-sharing octahedra (MO_6) are presented in Fig. 2e. Furthermore, Fig. 2f shows the Raman spectra used to examine the degree of disorder and vibrational energy modes in both samples. The band observed at *ca.* 290 cm^{-1} is attributed to O–W–O deformation and the one around 800 cm^{-1} corresponds to the stretching mode of O–W–O.[21] The bands occurring in between 380 and 800 cm^{-1} are associated with the stretching modes inside the NbO_6 octahedra.[22] Two more peaks at *ca.* 900 and 975 cm^{-1} may correspond to the WO_6 and NbO_6 octahedra, respectively.[23] Additionally, Raman spectroscopy allows for the use of the D band to G band intensity ratio (I_D/I_G) as a metric to evaluate the degree of disorder and defects in carbon-based materials. The structural defects can increase the ion and electron accessibility through the enhanced surface area and porosity of carbon materials.[24] In this case, the graphitic structure is characterized by the G band at *ca.* 1580 cm^{-1}, whereas the disorder-induced vibrations give rise to the D band at about 1380 cm^{-1}, showing the existence of defects. From Table 2, it is apparent that the I_D/I_G ratio of both materials is found to be close to 1, suggesting a

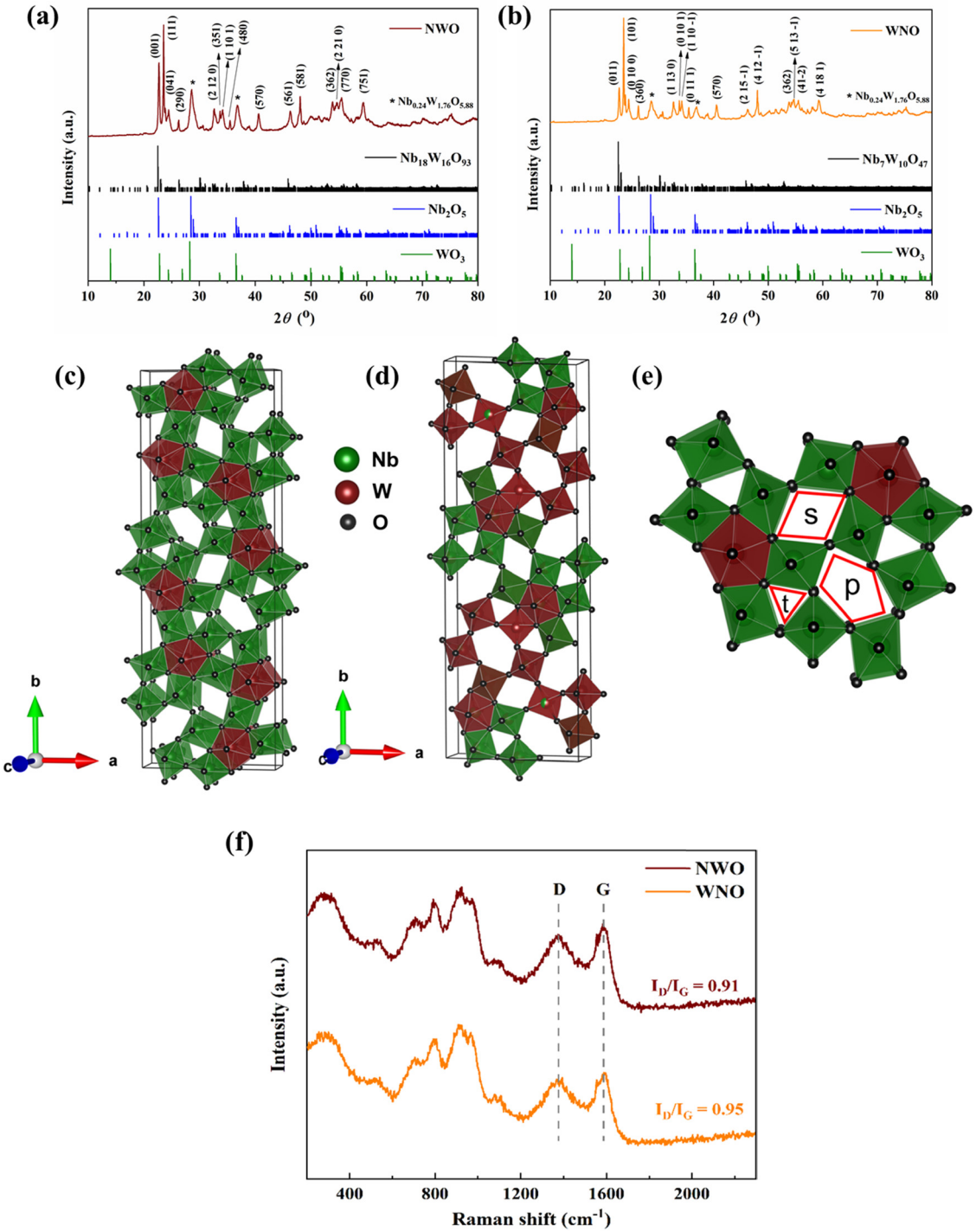

Fig. 2 XRD patterns (a) and (b) and crystal structures (c) and (d) of NWO and WNO materials, (e) representation of trigonal (t), square (s), and pentagonal (p) tunnels in NWO, and (f) Raman spectra of NWO and WNO materials.

significant number of defects, such as vacancies, edges, and other structural imperfections in the materials. Thus, the amorphous nature of the carbon-coated samples, introduced by the structural defects, can significantly enhance the electronic conductivity of the niobium tungsten oxide materials.

SEM and TEM were used to examine the morphology and microstructure of the NWO and WNO materials (Fig. 3). It is evident from Fig. 3a and d that both samples contain irregularly shaped and micron-sized particles. The particles exhibit porous surfaces, which may enhance electrolyte penetration and ion diffusion. The selected area electron diffraction (SAED) pattern shows the crystal orientations of NWO (inset: Fig. 3b) and WNO (inset: Fig. 3e) materials. In particular, the bright spots and the hollow ring pattern observed in the SAED images

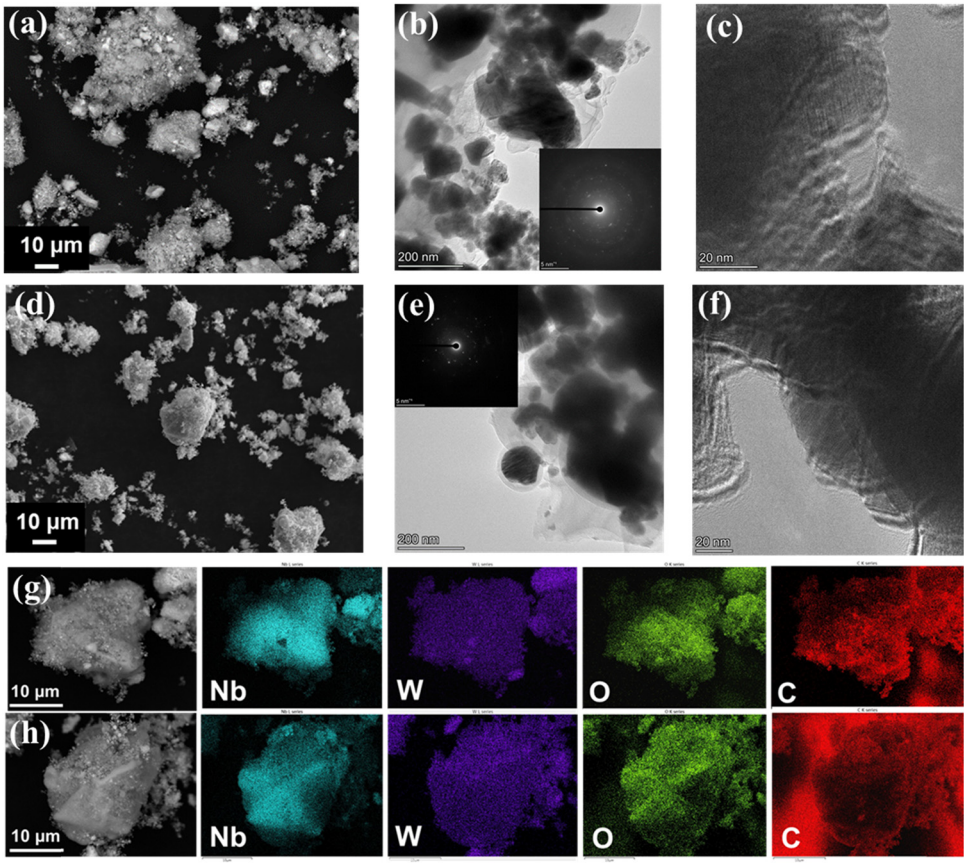

Fig. 3 SEM (a) and (d), TEM (b) and (e) and high-resolution transmission electron microscopy (HRTEM) (c) and (f) images of (a)–(c) NWO and (d)–(f) WNO samples (inset: SAED pattern), and EDX images of (g) NWO and (h) WNO materials.

suggest that the active particles are surrounded by an amorphous or disordered carbon framework.[25,26] The carbon-coating, thus, prevents the particle agglomeration and improves the electronic pathways. The HRTEM images (Fig. 3c and f) further reveal the well-resolved lattice fringes in both materials, demonstrating their crystalline nature. Thus, the thin amorphous layer that surrounds the active particles in the HRTEM images indicates that the niobium tungsten oxides have been successfully integrated and adorned with the carbon matrix. Finally, the homogeneous distribution of the elements, Nb, W, O, and C in both carbon-coated materials is confirmed by the EDX elemental mapping images, which are seen in Fig. 3g and h. Here, phase separation and/or element-rich clusters are not observed, confirming the effective integration of elements.

XPS analysis was used to identify the valence states and surface characteristics of NWO and WNO samples and the presence of elements, Nb, W, O and C in both samples is confirmed by XPS survey spectra (Fig. 4a). Furthermore, two main peaks, that appeared in Fig. 4b at 207.5 and 210.2 eV, correspond to Nb $3d_{5/2}$ and $3d_{3/2}$, respectively.[27] The XPS spectra of W (Fig. 4c) exhibit characteristic peaks at 35.7 and 38.0 eV, which are assigned to the W^{6+} $4f_{7/2}$ and $4f_{5/2}$, spin–orbit components, respectively. In addition, the peaks located at 34.1 and 36.4 eV correspond to the W^{5+} $4f_{7/2}$ and $4f_{5/2}$ states. Here, the presence of W^{5+} indicates partial reduction of tungsten, which may enhance the electronic conductivity by generating oxygen vacancies and defect sites that facilitate charge transport.[28] In both samples, the O 1s peak (Fig. 4d) deconvolutes into three peaks, metal–oxide (M = O), C–OH/C–O–C, and C═O, which are centered at binding energies of 530.5, 531.9 and 533.1 eV, respectively. Finally, a high-resolution C 1s XPS spectrum (Fig. 4e) consists of C–C, C–OH, C–O–C, O–C═O, and π–π* peaks at 284.4, 285.8, 286.9, 288.2, and 290.5 eV, respectively.[27]

The surface area and porosity of the synthesized NWO and WNO samples were measured using N_2 adsorption–desorption isotherms (Fig. 4f and g). The NWO sample had a specific surface area of 68.35 $m^2\ g^{-1}$, while the WNO sample had a specific surface area of 66.64 $m^2\ g^{-1}$, and both of the samples possess similar micropore volumes of 0.0242 $cm^3\ g^{-1}$. It was reported previously that the carbon coating can effectively reduce the agglomeration of bulk materials and enhance the surface area of the samples.[29] As a result, it increases the number of active sites for ion adsorption, as well as enabling easy and free transportation of electrolyte ions through the formation of aligned pore channels.[30] Furthermore, the Barrett–Joyner–Halenda (BJH) mean pore diameters (Fig. 4g) of the NWO and WNO samples are found to be 6.2 and 5.3 nm, respectively. Thus, the structures with wide surface areas can mitigate the evolution of stress produced during the ion insertion/extraction process, buffer volume change, and shorten the transport distance for ion diffusion.[30]

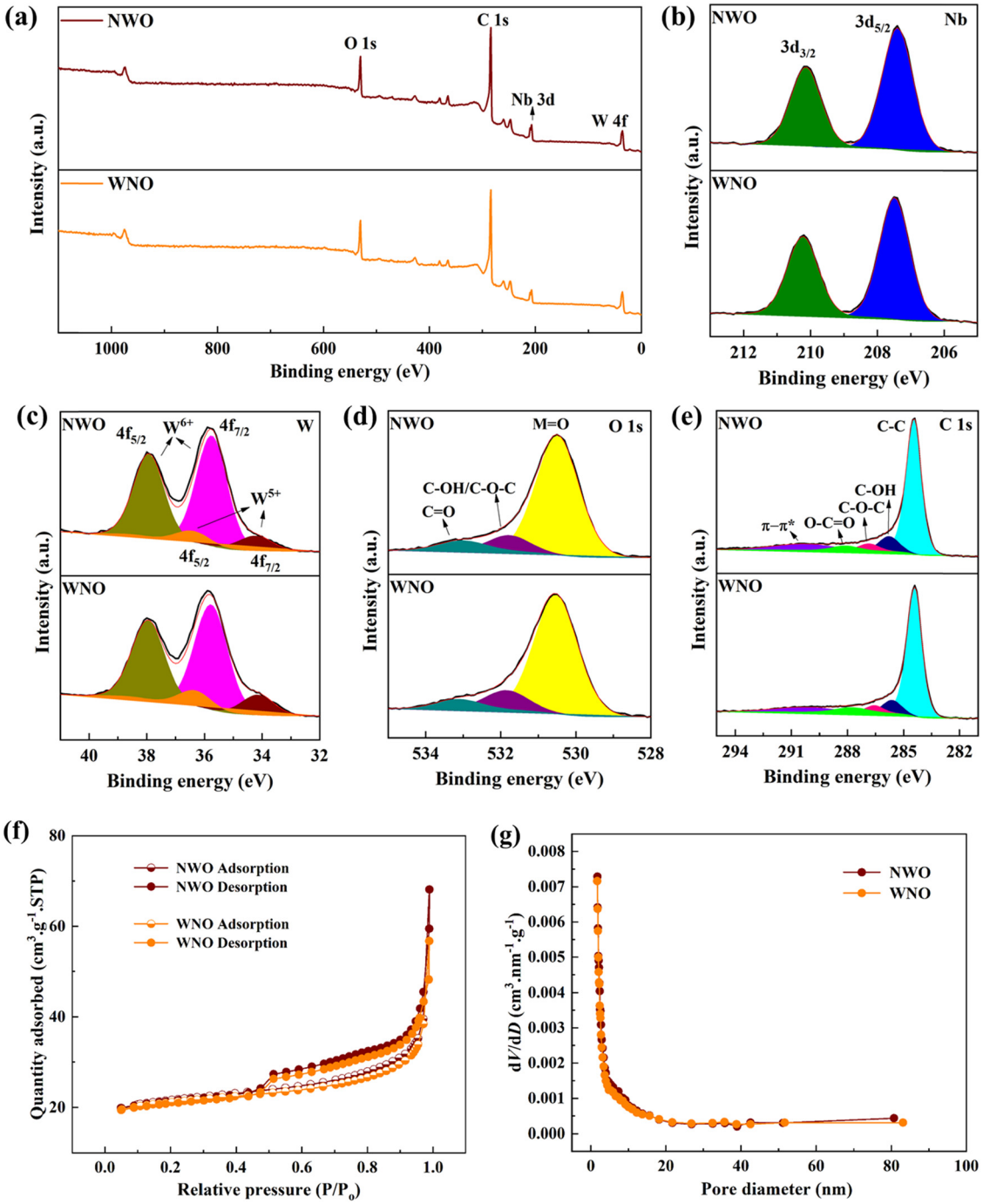

Fig. 4 (a) XPS survey spectra, (b) Nb 3d, (c) W 4f, (d) O 1s and (e) C 1s spectra, (f) N_2-adsorption and desorption isotherms, and (g) pore size distribution of NWO and WNO materials.

The cyclic voltammogram curves for NWO and WNO electrodes for the three initial cycles, in the voltage range of 0.01 to 2.5 V, at a scan rate of 0.2 mV s^{-1} are displayed in Fig. 5a and b. A pair of sharp redox peaks appearing near 0.1 V in both materials are attributed to the insertion and extraction process of Na. A broad reduction peak appearing near 0.6 V is due to the irreversible reaction of the electrolyte, which leads to the formation of the solid–electrolyte interface (SEI) layer on the electrode surface in both samples.[27] However, significant stability is maintained during the subsequent cycles, which is evident from the overlapping CV traces. Furthermore, Fig. 5c and d demonstrate the electrochemical performance of both samples at a current density of 10 mA g^{-1} for the initial three charge–discharge cycles. The NWO electrode exhibited high initial discharge/charge specific capacities of 265.5/161.3 mA h g^{-1}, respectively, while the WNO electrode delivered initial discharge/charge capacities of 206.7/122.5 mA h g^{-1}, respectively. Here, both materials exhibited a low initial coulombic efficiency (ICE) of *ca.* 60%, and it could be

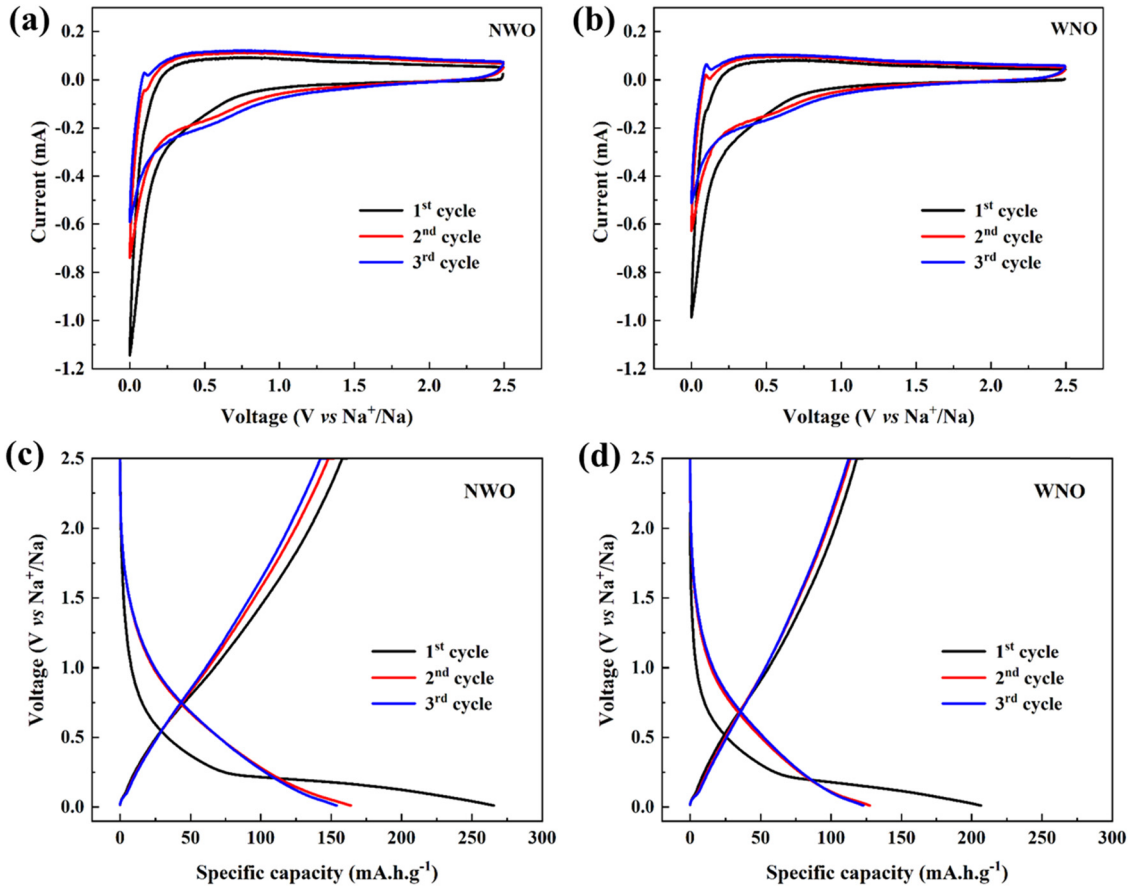

Fig. 5 CV curves of (a) NWO and (b) WNO materials for the initial three cycles at a scan rate of 0.2 mV s^{-1}, and galvanostatic charge/discharge curves for (c) NWO and (d) WNO materials for the first three cycles at a current density of 10 mA g^{-1}.

due to their large specific surface areas (Table 2), which influences the development of an SEI layer during the first cycle. As a result, a significant irreversible capacity loss occurs in the first cycle; however, both materials displayed greatly improved electrochemical performance during the subsequent cycles by recording high coulombic efficiencies of *ca.* 95%.

Fig. 6a displays the rate performance of NWO and WNO electrodes at different current densities. The NWO sample delivered high discharge specific capacities of 163, 129, 110, 90, 71, 48, 31 and 14 mA h g^{-1} at current densities of 10, 25, 50, 100, 200, 500, 1000, and 2000 mA g^{-1}, respectively, whereas, WNO delivered the discharge specific capacities of 127, 111, 99, 85, 69, 47, 28 and 11 mA h g^{-1}, respectively, at the same current densities. Here, at low current densities, NWO delivered slightly higher specific capacities compared to WNO, probably due to a small difference in their specific surface area (S_{BET}) and mean pore diameter (Fig. 4a and b). However, at higher current rates, both materials delivered nearly similar discharge capacities. It may instead arise from limited Na^+-ion diffusion and electrochemical kinetics, which dominate in both cases, rather than from the specific material properties of the electrodes. Cycling at high current rates does not damage the structure of either of the carbon-coated electrodes, since a considerable amount of specific capacity is still retained even when the current density is restored to 10 mA g^{-1}, which indicates superior rate performance for both samples. Thus, better reversibility and stability are attained in the WNO sample (84%), compared to NWO (72%).

Furthermore, at a current density of 100 mA g^{-1} the electrochemical performance of both samples is observed for long-term cycling (Fig. 6b). After 420 cycles, the NWO electrode delivered a discharge specific capacity of 72 mA h g^{-1}, which only represents a capacity retention of 69%. In contrast, WNO (76 mA h g^{-1}) demonstrated an impressive capacity retention of 81% even after 420 cycles. Nonetheless, the coulombic efficiency of both materials is nearly 100%. This study employed a relatively low electrode loading to investigate the intrinsic properties of the materials. Future work will focus on optimizing electrode fabrication to achieve higher mass loadings and validate the practical application potential in full-cell configurations.

Now, the electrochemical performances of NWO and WNO samples are compared with that of some other reported niobium and/or tungsten based anode materials for SIBs in Table 1. As summarized in Table 1, the present materials demonstrate competitive electrochemical performance compared to previously reported niobium/tungsten-based oxide anodes. In particular, they exhibit improved cycling stability with minimal capacity fading over prolonged cycles, indicating excellent structural robustness during repeated sodiation/desodiation. Additionally, the materials deliver favorable rate capability, retaining a significant fraction of the capacity even at higher

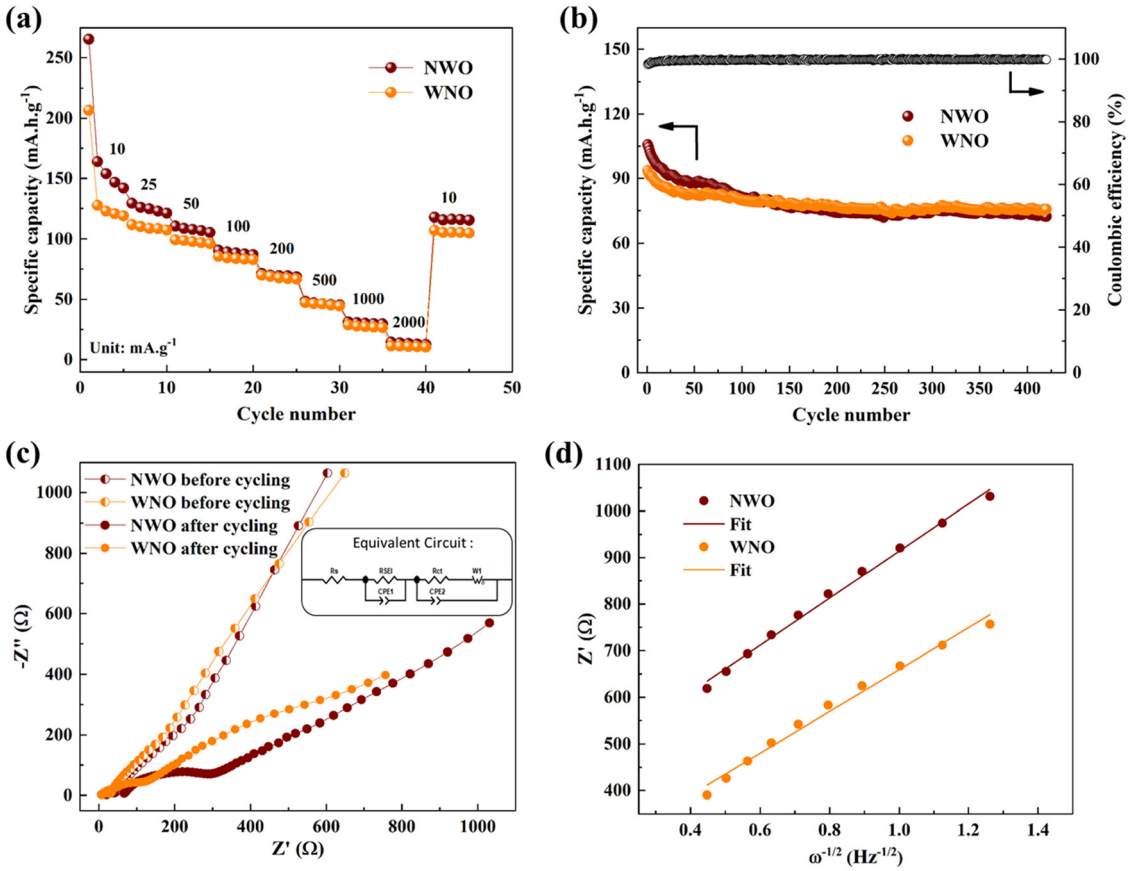

Fig. 6 (a) Rate capability at different current densities, (b) long-term cycling performance at a current density of 100 mA g^{-1}, (c) EIS, before and after cycling (inset: equivalent circuit), and (d) fitting curves of Z' *vs.* $\omega^{-1/2}$ at a low frequency region of NWO and WNO samples.

Table 1 Comparison of electrochemical performances of NWO and WNO samples with the other reported Nb/W based anode materials for SIBs

Material	Preparation	Potential window (V *vs.* Na^+/Na)	Current density (mA g^{-1})	Number of cycles	Capacity retention (%)	Ref.
NbO_2	Solid-state method	0.01–2.5	50	500	70	31
Nb_2O_5@WS_2@C	Electrospinning-Hydrothermal	0.01–3.0	1000	200	62	32
Nb–Ti octahedral molecular sieves (Cd-NTO)	Hydrothermal	0.01–2.5	50	100	72	33
W-Nb_2O_5/C	Hydrothermal	0.01–3.0	100	100	70	34
NWO	Hydrothermal	0.01–2.5	100	420	69	This work
WNO	Hydrothermal	0.01–2.5	100	420	81	This work

current densities, which highlights their fast charge transport kinetics. These advantages can be attributed to the optimized composition and microstructure, which facilitate efficient ion diffusion and enhanced electronic conductivity.

Analysis by electrochemical impedance spectroscopy (Fig. 6c) provides a clear understanding of the high and stable performance observed in the WNO sample. An equivalent circuit, used to match the Nyquist plots for both samples, before and after 20 cycles is shown in the inset of Fig. 6c, and it consists of a solution resistance (R_s), SEI layer resistance (R_{SEI}), and a charge transfer resistance (R_{ct}). Both NWO and WNO electrodes exhibited similar charge transfer resistances of *ca.* 30 Ω before cycling. However, a very high charge transfer resistance of 329.7 Ω is recorded for the NWO sample compared to that of WNO (172.5 Ω), after 20 cycles. This may be the key to the slow capacity fading seen in the case of NWO. Thus, the electrochemical performance of carbon-coated samples is influenced by SEI/charge transfer resistance during long-term cycling.

Table 2 Comparison of the I_D/I_G ratio, specific surface area (S_{BET}), reversible discharge capacity at 10 mA g^{-1}, charge transfer resistance (R_{ct}) after 20 cycles and the Na^+-ion diffusion coefficient for NWO and WNO samples

Material	I_D/I_G	S_{BET} (m^2 g^{-1})	Discharge capacity at 10 mA g^{-1} (mA h g^{-1})	R_{ct} (Ω)	Diffusion coefficient (cm^2 s^{-1})
NWO	0.91	68.35	163.95	329.7	6.4×10^{-14}
WNO	0.95	66.64	127.55	172.5	8.2×10^{-14}

Additionally, eqn (1) can be used to compute the Na^+-ion diffusion coefficient, D_{Na^+}, which is directly related to the electrochemical stability and the charge transfer resistance.[35]

$$D_{Na^+} = \frac{R^2T^2}{2A^2n^4F^4C_{Na}{}^2\sigma^2} \quad (1)$$

where R is the gas constant, T is the temperature, A is the effective working area of the electrode, n is the number of transferred electrons, F is the Faraday constant, C represents the Na^+-ion concentration, and σ is the slope of Z' *vs.* $\omega^{-1/2}$, which is obtained using eqn (2),

$$Z' = R_s + R_{SEI} + R_{ct} + \sigma\omega^{-1/2} \quad (2)$$

Here, the slope (σ) can be calculated by using the plot between Z' and $\omega^{-1/2}$ (Fig. 6d). Z' is the real part of impedance, σ is the Warburg factor, and ω is the angular frequency.[36] The NWO electrode exhibited a Na^+-ion diffusion coefficient of 6.4×10^{-14} cm^2 s^{-1}, comparable with the reported value for

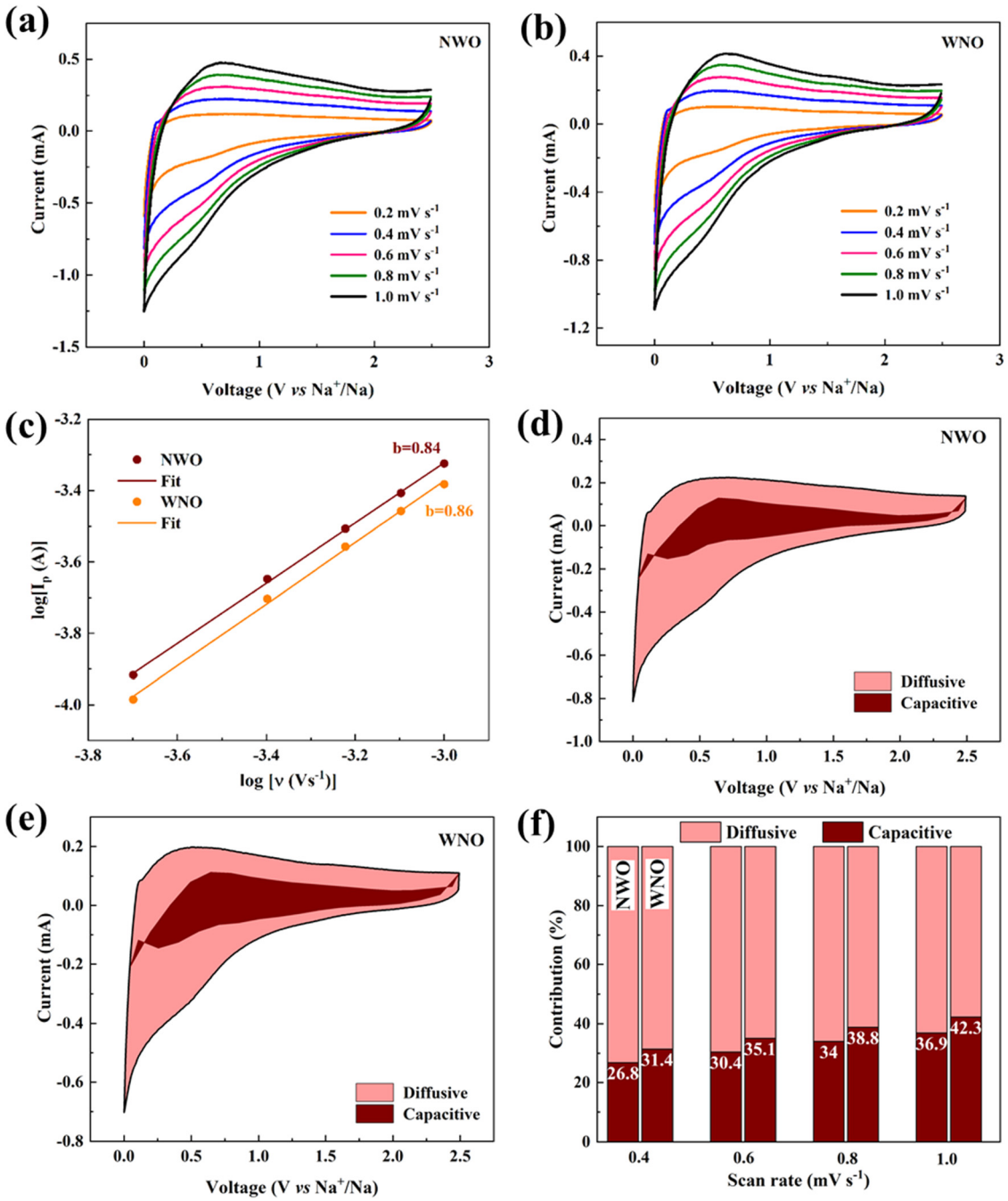

Fig. 7 CV curves at different scan rates for (a) NWO and (b) WNO materials, (c) the logarithmic relationship between the scan rates and peak currents in NWO and WNO materials, the CV curve showing the diffusion-controlled and capacitive contributions in (d) NWO and (e) WNO materials at a scan rate of 0.4 mV s^{-1}, and (f) contribution ratio of diffusion-controlled and capacitive processes to the total capacity at different scan rates for NWO and WNO materials.

Nb_2O_5,[37] after all the values were substituted, while the WNO electrode exhibited a significantly higher Na^+-ion diffusion coefficient of 8.2×10^{-14} cm^2 s^{-1}. Thus, the transfer of Na^+-ions is a little bit faster in the case of WNO.

Fig. 7a and b display the CV plots of the NWO and WNO materials at different scan rates. In both materials, the anodic and cathodic peak currents increase with increased scan rate, and the enhanced reversibility is demonstrated by their improved redox peak symmetry. Additionally, a small shift in the oxidation peak positions toward positive potential indicates that both electrode materials have less polarization.[38]

The electrode dynamics in both materials are better examined using the power law relationship using eqn (3),[27]

$$i_p = a\nu^b \quad (3)$$

Here i_p is the peak current, ν is the scan rate, and a and b are arbitrary constants obtained from the fitting. Now, eqn (3) can be modified as eqn (4).

$$\log(i_p) = \log(a) + b\log(\nu) \quad (4)$$

In this case, the capacitive and diffusion-controlled contributions can be evaluated using the slope b, which can be computed from a linear fit of the plot between $\log(\nu)$ and $\log(i_p)$ (Fig. 7c). According to Fig. 7c, the b values of NWO and WNO materials are found to be 0.84 and 0.86, respectively, suggesting that both capacitive and diffusive processes govern the sodium ion storage mechanism. Furthermore, eqn (5) provides the quantitative distribution of the diffusive and capacitive contributions to the overall storage mechanism in both materials.[27]

$$i(V) = k_1\nu + k_2\nu^{1/2} \quad (5)$$

Here, the surface capacitive and diffusion-controlled contributions are denoted by $k_1\nu$ and $k_2\nu^{1/2}$, respectively. Fig. 7d and e display the capacitive and diffusive contributions on the CV plots of the NWO and WNO electrodes, respectively, at a scan rate of 0.4 mV s^{-1}. Fig. 7f makes it evident that, in both materials the fraction of capacitive contribution gradually rises as the scan rate increases from 0.4 to 1 mV s^{-1}. This is because under higher rate conditions, surface capacitance dominates the total capacity. Concurrently, the diffusion-regulated capacity contribution decreases because the slow intercalation speed is unable to satisfy the needs of the high rate of electrochemical processes at higher scan rates.[39] Thus, the carbon-coated materials, NWO and WNO, delivered enhanced electrochemical performance because of their improved structural defects, large specific surface areas, pore sizes and high Na^+-ion diffusion coefficients.

4. Conclusions

The present work proposes carbon-coated, TTB-type niobium tungstates, $Nb_{18}W_{16}O_{93}$ and $Nb_7W_{10}O_{47}$, as new sodium insertion materials. The anode materials were successfully synthesized *via* a facile hydrothermal-annealing process. As a result, the Nb-rich carbon-coated material, NWO, demonstrated a high discharge capacity of 163.95 mA h g^{-1} at 10 mA g^{-1}, whereas the W-rich material, WNO, achieved a significant capacity retention of more than 81%. Here, the Nb-dominant material exhibited different charge/discharge profiles, and a slightly higher specific capacity may be due to more sites available for sodium, but the W-dominant material exhibited better structural stability and more consistent performance possibly due to being a more readily confirmed stable phase. The slow capacity fading observed in the material, NWO, was explained with respect to its higher charge transfer resistance compared to WNO. Niobium tungsten oxides are thus highlighted in this paper as intriguing anode options for the advancement of high-performance SIB technology.

Author contributions

Y. Bhaskara Rao: investigation, methodology, conceptualization, formal analysis, data curation, and writing – original draft. Katta Vamsi Krishna: investigation and visualization. C. André Ohlin: validation, supervision, resources, visualization, funding acquisition, writing – review & editing, and project administration.

Conflicts of interest

The authors declare no competing financial interest.

Data availability

Any data that support the findings of this study are included within the article.

Acknowledgements

The authors are thankful to the Kempe foundation (JCSMK22-0094 and JCSMK24-511) and the Swedish Research Council (VR 2023-04608) for financial support and acknowledge the Multipurpose Adaptive X-ray Scattering platform (MAXS) for instrument access and technical support and Umeå Centre for Electron Microscopy (UCEM) for the facilities and technical assistance at the Chemical Biological Centre (KBC), Umeå University, SWEDEN. The authors also thank Dr Solomon Tesfalidet (UmU) for invaluable technical assistance.

References

1 Z. Xue, S. Yang, S. Zhang, L. Xing, S. Lee, H. S. Park, C. Yan and J. Huang, *Energy Mater. Adv.*, 2025, **6**, 0415.
2 J. Bai, Z. Li, X. Wang, S. Konrad, C. Wu and H. Zhao, *Energy Mater. Adv.*, 2024, **5**, 0086.
3 M. Chen, Q. Liu, S. Wang, E. Wang, X. Guo and S. Chou, *Adv. Energy Mater.*, 2019, **9**, 1803609.
4 D. Fan, Q. Shen, H. Li, X. Qu, L. Jiao and Y. Liu, *Energy Mater. Adv.*, 2024, **5**, 0073.
5 E. Irisarri, A. Ponrouch and M. R. Palacin, *J. Electrochem. Soc.*, 2015, **162**, A2476–A2482.

6 H. Kang, Y. Liu, K. Cao, Y. Zhao, L. Jiao, Y. Wang and H. Yuan, *J. Mater. Chem. A*, 2015, **3**, 17899–17913.
7 Q. Deng, Y. Fu, C. Zhu and Y. Yu, *Small*, 2019, **15**, 1804884.
8 S. Y. Lee, A. S. Lim, Y. M. Kwon, K. Y. Cho and S. Yoon, *Inorg. Chem. Front.*, 2020, **7**, 3176–3183.
9 H. Li and H. Zhou, *Chem. Commun.*, 2012, **48**, 1201–1217.
10 Y. B. Rao and C. A. Ohlin, *Sustainable Energy Fuels*, 2025, **9**, 2217–2227.
11 G. Chen, J. Chen, I. P. Parkin, G. He and T. S. Miller, *ChemElectroChem*, 2022, **9**, e202200800.
12 Y. Subramanian, G. K. Veerasubramani, M. S. Park and D. W. Kim, *Mater. Lett.*, 2022, **314**, 131891.
13 K. J. Griffith, K. M. Wiaderek, G. Cibin, L. E. Marbella and C. P. Grey, *Nature*, 2018, **559**, 556–563.
14 C. P. Kocer, K. J. Griffith, C. P. Grey and A. J. Morris, *Chem. Mater.*, 2020, **32**, 3980–3989.
15 F. Krumeich, *Crystals*, 2021, **11**, 1514.
16 F. Krumeich and M. Worle, *Z. Anorg. Allg. Chem.*, 2025, **651**, e202500033.
17 S. Nagendran, B. Wen, C. P. Grey, S. Nagendran, A. Mahadevegowda, S. Vema and M. Danaie, *Matter*, 2024, **7**, 3567–3586.
18 C. Cai, P. McCormack, Z. Nie and G. M. Koenig Jr, *J. Electrochem. Sci. Eng.*, 2023, **13**, 641–658.
19 R. Xia, C. Sun, Y. Wang, D. M. Cunha, H. Peng, K. Zhao, M. Huijben and J. E. ten Elshof, *J. Power Sources*, 2021, **482**, 228898.
20 F. Krumeich, M. Worle and A. Hussain, *J. Solid State Chem.*, 2000, **149**, 428–433.
21 C. Yue, X. Zhu, M. Rigutto and E. Hensen, *Appl. Catal., B*, 2015, **163**, 370–381.
22 Y. B. Rao and C. A. Ohlin, *RSC Adv.*, 2025, **15**, 34300–34309.
23 Y. Yang, H. Zhu, J. Xiao, H. Geng, Y. Zhang, J. Zhao, G. Li, X. L. Wang, C. C. Li and Q. Liu, *Adv. Mater.*, 2020, **32**, 1905295.
24 R. Hou, B. Liu, Y. Sun, L. Liu, J. Meng, M. D. Levi, H. Ji and X. Yan, *Nano Energy*, 2020, **72**, 104728.
25 Y. Da Cho, G. T. K. Fey and H. M. Kao, *J. Power Sources*, 2009, **189**, 256–262.
26 C. Corbella, E. Bertran, M. C. Polo, E. Pascual and J. L. Andujar, *Diamond Relat. Mater.*, 2007, **16**, 1828–1834.
27 Y. Bhaskara Rao, N. Tavajohi and C. Andre Ohlin, *Batteries Supercaps*, 2025, **8**, e202500134.
28 S. Shetty, R. Karmakar, S. D. Sutar, S. Narayanasamy, S. Aravind, A. Swami and S. Sinha, *ACS Appl. Nano Mater.*, 2025, **8**, 23308–23325.
29 Y. Xia, M. Yoshio and H. Noguchi, *Electrochim. Acta*, 2006, **52**, 240–245.
30 A. Safartoobi, J. Mazloom and F. E. Ghodsi, *J. Energy Storage*, 2023, **68**, 107818.
31 P. Chithaiah, R. C. Sahoo, J. H. Seok, S. U. Lee, H. S. S. R. Matte and C. N. R. Rao, *ACS Appl. Mater. Interfaces*, 2023, **15**, 45868–45875.
32 Y. Zhao, Z. Feng, Y. Tan, Q. Deng and L. Yao, *Nanomaterials*, 2024, **14**, 631.
33 Y. B. Rao, N. Tavajohi and C. A. Ohlin, *Mater. Adv.*, 2026, **7**, 1691–1703.
34 C. J. Y. X. Liu Ya-ting, Li Li-bing, Li Xin-xin and Miao Yong-xia, *Mod. Chem. Ind.*, 2025, **45**, 163–170.
35 S. Khatua, K. R. Achary, Y. B. Rao, K. Sasikumar, A. K. Samal and L. N. Patro, *New J. Chem.*, 2024, **48**, 18277–18290.
36 C. Liu, N. Xiao, Y. Wang, H. Li, G. Wang, Q. Dong, J. Bai, J. Xiao and J. Qiu, *Fuel Process. Technol.*, 2018, **180**, 173–179.
37 J. Ni, W. Wang, C. Wu, H. Liang, J. Maier, Y. Yu and L. Li, *Adv. Mater.*, 2017, **29**, 1605607.
38 B. He, J. Cunha, Z. Hou, G. Li and H. Yin, *J. Colloid Interface Sci.*, 2023, **650**, 857–864.
39 S. Li, J. Qiu, C. Lai, M. Ling, H. Zhao and S. Zhang, *Nano Energy*, 2015, **12**, 224–230.